Erschienen in: Solar Energy Materials and Solar Cells ; 172 (2017). - S. 335-340
https://dx.doi.org/10.1016/j.solmat.2017.07.046

Hybrid solar cells from Sb_2S_3 nanoparticle ink

Wei Wang, Frank Strössner, Eugen Zimmermann, Lukas Schmidt-Mende*

A B S T R A C T

Sb_2S_3 is a promising candidate for solar cell absorbers due to its high absorption coefficient, suitable band gap and earth-abundant constituents. Here we present the preparation of hybrid solar cells from an ink of colloidal Sb_2S_3 nanoparticles and P3HT. Colloidal Sb_2S_3 nanoparticles were prepared via hot injection method. Solar cells based on these nanoparticles achieves a power conversion efficiency of 1.5%, which is efficiency record for planar hybrid solar cells based on Sb_2S_3 nanoparticles. We investigated in detail the role of the capping agents on the performance of solar cells.

1. Introduction

Hybrid solar cells (HSCs) have sparked widespread interest due to its unique characteristics such as cost reduction in device fabrication, tailored energy level alignment, stability, etc. For HSCs, light absorption takes place in a semiconductor sensitizer sandwiched usually between a thin layer of n-type metal-oxide and a p-type organic hole transport material (HTM). Several classes of semiconducting materials, with strong absorption of incident light, large dielectric constant and high charge carrier mobility have been investigated as sensitizer for HSCs. Examples for widely used sensitizers for HSCs are lead sulfide (PbS) [1], copper zinc tin selenide (CZTS) [2], indium gallium selenide (CIGS) [3], organic–inorganic hybrid perovskite [4] and antimony sulfide (Sb_2S_3). Among these materials, Sb_2S_3 has emerged as one of the most promising candidate in solar cell application due to its high absorption coefficient ($1.8\times10^5 cm^{-1}$ at 450 nm), suitable bandgap (1.7 eV) [5], as well as earth-abundancy and assumed reduced toxicity.

Sb_2S_3 films are commonly fabricated via chemical bath deposition (CBD) or atomic layer deposition (ALD). With these methods, amorphous Sb_2S_3 films (bandgap 2.15 eV) with desired thickness are formed on the substrates at initial processing stage and then converted to crystalline stibnite (bandgap 1.75 eV) by a subsequent annealing process. By choosing different HTMs, such as poly(3-hexylthiophene) (P3HT), poly[2,6-(4,4-bis-(2-ethylhexyl)-4H-cyclo-penta[2,1-b;3,4-b'] dithiophene)-alt-4,7(2,1,3-benzothiadiazole)] (PCPDTBT), 2,2′,7,7′-tetrakis(N,N-di-p-methoxyphenylamine)-9,9′-spirobi-fluorene (spiroOMeTAD) and CuSCN, and optimization of film forming parameters and treatment, strong progress has been made for Sb_2S_3 sensitized HSCs. To date, the highest efficiency of Sb_2S_3 sensitized HSCs has achieved 7.5% utilizing CBD [6]. However, CBD method will always introduce undesired impurities and defects in the structure such as oxide. This method is also considered not suitable for large scale industrial application. ALD method, on the other hand, has achieved 5.8% efficiency with a planar Au/P3HT/ALD- Sb_2S_3/bl-TiO2/FTO architecture [7].

For industrial applications it is desirable to have a scalable, energy efficient, and reproducible deposition method for such an absorber layer. Using an "ink" of dispersed Sb_2S_3 nanoparticles to prepare the absorber layer allows the deposition by commonly used coating techniques that allow low-cost and mass-production. Therefore such a deposition method seems very attractive for solar cells applications. To our knowledge there is only one report, where Sb_2S_3 nanoparticles have been used to prepare hybrid solar cells [8]. Ideally the processing could be done at low temperatures, applicable for plastic substrates, such as PET or PEN. However, currently we need a minimum annealing temperature of > 250 °C, which is above the possible processing temperature of such plastic substrates.

In this work, we firstly report on synthesis of colloidal Sb_2S_3 nanoparticles (NPs) capped with 1-dodecanethiol (DT) molecules by hot-injection method, and on the application of pre-synthesized Sb_2S_3 NPs in planar hybrid solar cells. Due to the adoption of hot injection method, it typically only takes a few minutes to grow out Sb_2S_3 NPs with controlled sizes in solution. All precursor materials used in the reaction are air stable and inexpensive, which makes the synthesis facile to be implemented. Normally, Oleic acid (OA) is adopted as surfactant to stabilize the nanoparticles synthesized by hot-injection method [9]. The long chains of OA (18 carbons) ligands ensures the solution processability and surface passivation of the NPs. Unfortunately, the presence of the electrically insulating OA molecules at the nanoparticle surface will prevent efficient charge separation and

* Corresponding author.
E-mail address: Lukas.Schmidt-Mende@uni-konstanz.de (L. Schmidt-Mende).

Konstanzer Online-Publikations-System (KOPS)
URL: http://nbn-resolving.de/urn:nbn:de:bsz:352-0-426314

charge transportation between particles assembled in thin film for e.g. photovoltaic devices [10]. In this work, we used as capping agent a short chain 1-dodecanethiol (12 carbons) for our Sb_2S_3 NPs. We achieved a stable nanoparticle "ink", which has been used to prepare thin Sb_2S_3 films. In combination with P3HT as HTM a solar conversion efficiency of 1.54% was obtained at AM 1.5 G with planar hybrid solar comprised of FTO/TiO_2/DT-capped Sb_2S_3/P3HT/Ag, whereas the control device with a configuration of FTO/TiO_2/OA-capped Sb_2S_3/P3HT/Ag yields an efficiency of only 0.3%. This shows the potential of using pre-synthesized Sb_2S_3 NPs in planar hybrid solar cells and the important role of the capping ligands.

2. Experimental

2.1. Synthesis and purification of Sb_2S_3 nanoparticles

2 mmol of antimony (III) acetate (Aldrich 99.99% trace metals basis), 20 ml of 1-octadecene (Aldrich 90% technical grade) and 10 ml of 1-dodecanethiol (Aldrich 98%) were mixed in a 100 ml three-necked round bottomed flask. The mixture was then heated to 185 °C for 60 min under N_2 atmosphere. The sulphur precursor was prepared by dissolving 6 mmol sulphur (Aldrich 99.998% trace metals basis) into 6 ml 1-octadecene under 140 °C. The sulphur precursor was then swiftly injected into the three-necked flask, and allowed the mixed solution to react for 2 min at 185 °C. Once the Sb_2S_3 nanoparticles were formed, 1.5 ml of isopropanol (Aldrich 99.5%) was added to cool down the solution. The synthesized orange-red coloured nanoparticles were purified by repeated centrifugation for three times with isopropanol and re-dispersion in 4 ml chlorobenzene (Aldrich 99.8% anhydrous). The Sb_2S_3 nanoparticles capped with oleic acid (Aldrich 90%) were prepared by an identical synthetic protocol except 20 ml of oleic acid was used instead of 1-dodecanethiol.

2.2. Device fabrication

F-doped SnO_2 (FTO, TCO1010, Solaronix) glass substrates were subsequently cleaned for 15 min each in ultrasonic baths of acetone and isopropyl. A 80 nm thick compact TiO_2 photoanode film was prepared by sputtering TiO_2 on the FTO substrates. 50 µl of Sb_2S_3 nanoparticles in chlorobenzene solution (50 mg/ml) was spin-coated on the TiO_2 covered FTO substrates in air at 3000 rpm for 60 s. Then the substrates were transferred to a glove box and annealed to 250–300 °C for 30 min. After cooling down to room temperature, the film was taken out of the glovebox and as HTM, P3HT (poly-3-hexylthiophene)/chlorobenzene solution (20 mg ml^{-1}) was then spin-coated on the Sb_2S_3 film at 1500 rpm for 2 min. A 130 nm thick Ag counter electrode was then deposited with thermal evaporation.

2.3. Device characterization

Absorption spectra were measured using an Agilent Cary 5000 UV–Vis–NIR spectrometer equipped with an integrating sphere. Scanning electron microscopy (SEM) pictures were acquired by Zeiss Neon 40ESB operated at 7.5 keV. Fourier transform infrared spectroscopy was carried out on Spectrum100 FTIR.

For current density-voltage measurements (J-V), all devices were illuminated with an AM 1.5 G solar simulator at a light intensity of about 110 mW cm^{-2}. The solar simulator was calibrated by a Fraunhofer ISE certified Si reference diode with an attached KG5 filter. Spectra were acquired with a Keithley 2410 source meter controlled by a Matlab program. The external quantum efficiency (EQE) was measured using a 150 W xenon lamp, an OMNI Lambda 300 monochromator, a Zurich Instruments Lock-In amplifier, and an LED source as white light background illumination. Solar cells were placed in a light tight sample holder (in order to avoid additional excitation of the active layer due to scattered light) and illuminated through a shadow mask defining three times an active area of 0.125 cm^2 for the three pixels on each substrate.

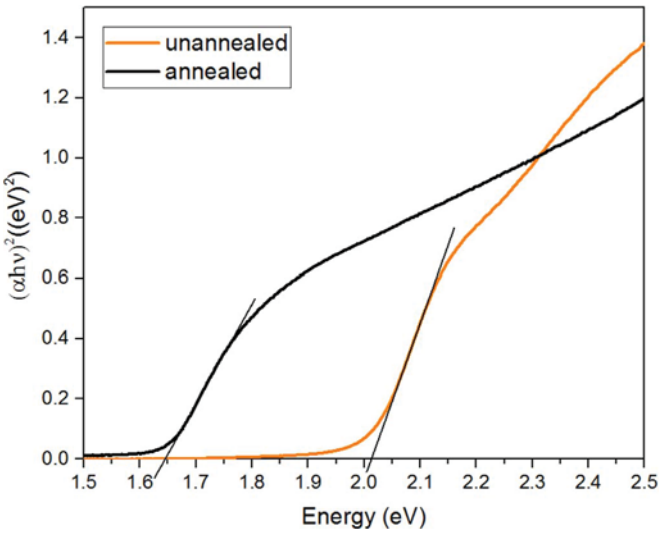

Fig. 1. Tauc plot of the optical absorption spectra of Sb_2S_3 NPs before (amorphous phase) and after annealing (crystalline phase). (For interpretation of the references to color in this figure legend, the reader is referred to the web version of this article.)

3. Result and discussion

For optical characterization, thin films were deposited on clean glass substrates. The colour of as deposited Sb_2S_3 films is originally orange-red, which changes to grey-black after annealing in N_2-atmosphere at 300 °C for 30 min. In Fig. 1 the Tauc plot of the Sb_2S_3 film before and after the annealing process is plotted. As an direct band gap semiconductor, the band gap of Sb_2S_3 can be obtained by the following formula: $\alpha hv = A(hv - E_g)^{1/2}$, where α, v, and E_g are the absorption coefficient, optical frequency and band gap [11,12]. The energy gap can then be calculated by analysing $(\alpha hv)^2$ as function of (hv). For unannealed samples, the sample colour is orange/red and its absorption edge is near 2.0 eV, which is consistent with the characters of amorphous Sb_2S_3. After annealing, the amorphous Sb_2S_3 is crystalized, which can be also observed on the colour change towards grey-black and the shift of absorption edge to 1.6 eV. According to Fig. 1, the energy gap is estimated to be 2.02 eV for the amorphous Sb_2S_3 and 1.65 eV for the crystallized Sb_2S_3. These results are consistent with previous reports [13,14].

The SEM images of Sb_2S_3 nanoparticles on TiO_2 covered FTO substrates before and after annealing are shown in Fig. 2. These images were recorded under same working distance (3 mm), acceleration voltage (7.5 keV), brightness (32%) and contrast (51%). Before annealing (Fig. 2a), the deposited Sb_2S_3 nanoparticles exhibited spherical shape. The diameter of as synthesized nanoparticles can be tuned from 80 nm to 570 nm by changing the synthesis parameter (see Fig. s1). The average diameter of the spherical Sb_2S_3 particles used in this study is approximately 150 nm as shown in (Fig. 2a). After 300 °C annealing for 30 min (Fig. 2b), it is evident that the Sb_2S_3 nanoparticles melted on the substrate, resulting the surface morphology being rearranged. However, the melting temperature of bulk Sb_2S_3 is 560 °C. The low melting temperature of the Sb_2S_3 nanoparticles in this work can be attributed to the 'quantum size effect', the depressed melting point due to reduced dimension of semiconductor particles [15,16]. The fused Sb_2S_3 nanoparticles in Fig. 2b exhibit less contrast with the TiO_2 covered FTO substrate, compared with those unannealed nanospheres in Fig. 2a. This might indicate that there was more charging effect in the unannealed sample than in the annealed one. In general, the charging effect is mainly caused by the electric charges accumulation on the specimen

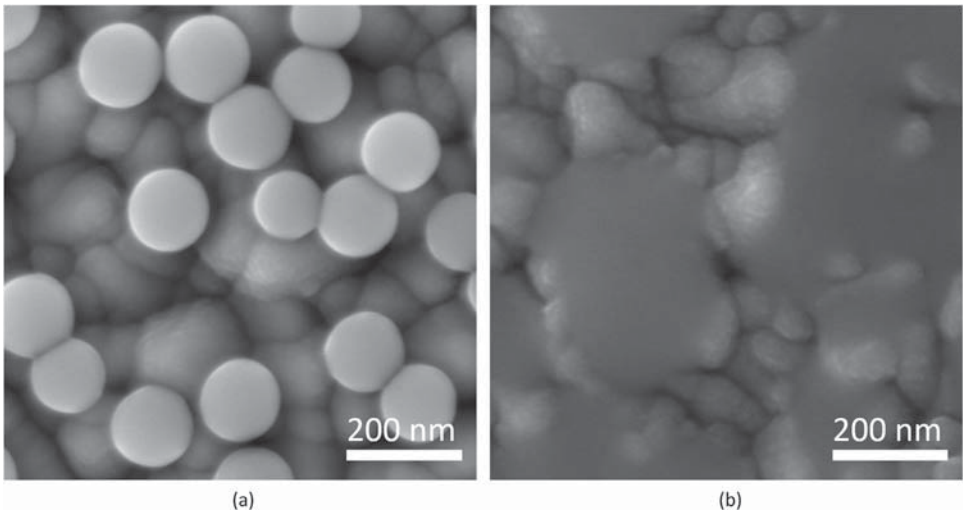

Fig. 2. SEM images of Sb_2S_3 NPs on TiO_2 covered FTO substrates (a) before and (b) after annealing.

surface [17]. It seems to indicate improved conductivity within the Sb_2S_3 and between Sb_2S_3 and the substrate compared to the non-annealed films.

In addition to the colour change from red-orange to grey-black, this also supports the transformation after annealing from the amorphous Sb_2S_3 into the more conductive, crystalline stibnite phase. It confirms the expectation, that annealing up to the melting point improves the contact area through morphological change and better wetting between Sb_2S_3 and TiO_2/FTO.

Fourier transform infrared measurements were carried out on the OA and DT capped Sb_2S_3 nanoparticles before and after the annealing process, as an effort to investigate absorption mechanism of the ligand molecules on the surface of Sb_2S_3 nanoparticles. Fig. 3a shows the FTIR spectra of Sb_2S_3 nanoparticles with OA ligands before and after 300 °C annealing for 30 min. Before annealing (red curve in Fig. 3a), two sharp bands at 2920 and 2850 cm^{-1} were attributed to the methylene C-H asymmetric and symmetric stretch, respectively, indicate the presence of OA on the Sb_2S_3 nanoparticles [18,19]. The weak C=O stretching vibration peak at 1710 cm^{-1} confirmed the formation of a chemical bond between Sb_2S_3 and OA [18]. Those FTIR peaks mentioned above were still clearly visible, even though largely weakened by the annealing process (black curve in Fig. 3a). This fact confirms the previous reports of only partial desorption of OA molecules under such an annealing process [20]. Fig. 3b depicts the FTIR spectra of Sb_2S_3 with DT ligands before and after annealing. Before annealing (red curve in Fig. 3b), two well-resolved peaks at 2915 and 2850 cm^{-1} appear, which are assigned to asymmetric and the symmetric stretch of the methylene group [21,22]. The sharp peaks at 1462 and 1377 cm^{-1} correspond to the methylene scissoring mode and methyl symmetric bending vibration, respectively [23]. The disappearance of the S-H stretching band at 2577 cm^{-1} in dodecanethiol molecules in solution as demonstrated by previous reports [23,24] confirms the bonding between Sb_2S_3 and DT. After annealing, those characteristic FTIR peaks of DT mentioned above disappear (black curve in Fig. 3b), indicating the complete desorption of DT molecules on Sb_2S_3 nanoparticles after this annealing treatment at 300 °C. This result from Fig. 3 can be attributed to the much lower boiling point of DT (266–285 °C, 1 atm), compared to OA (360 °C, 1 atm). This explains, why the DT capped Sb_2S_3 nanoparticles will be electrically much better connected after annealing as the OA capped Sb_2S_3, as in their case the capping agent is only partly removed and we still find isolating OA chains between the Sb_2S_3 nanostructures.

To compare the photovoltaic properties of OA and DT capped Sb_2S_3 solar cells (SCs), planar device architectures were constructed as shown in Fig. 4a. All devices were annealed at 300 °C for 30 min after Sb_2S_3 deposition. The band alignment of the solar cell is depicted in Fig. 4b.

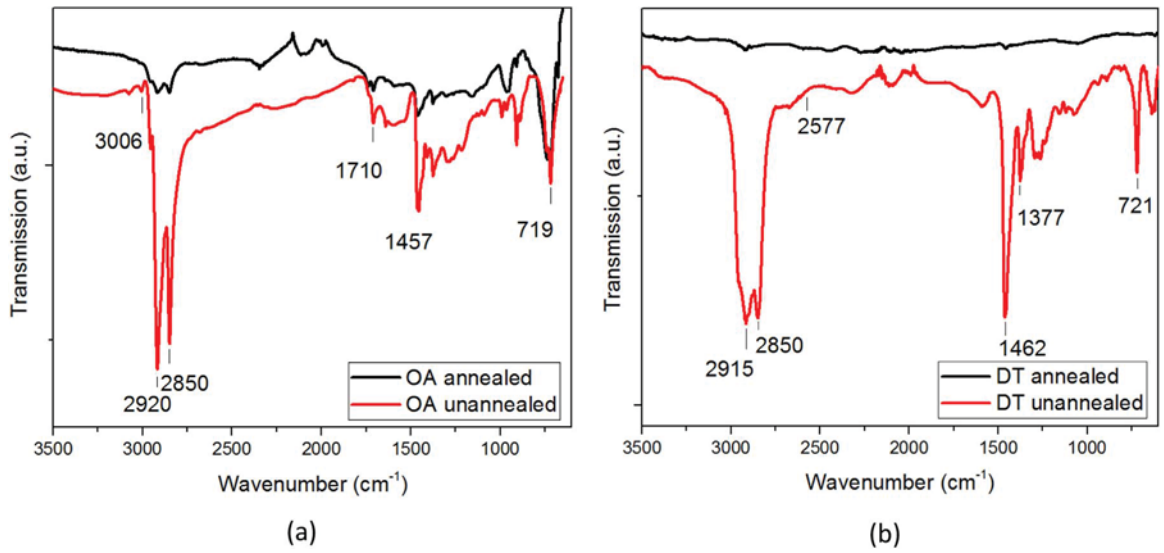

Fig. 3. The FTIR images of (a) OA and (b) DT capped Sb_2S_3 nanoparticles before (black) and after annealing (red). (For interpretation of the references to color in this figure legend, the reader is referred to the web version of this article.)

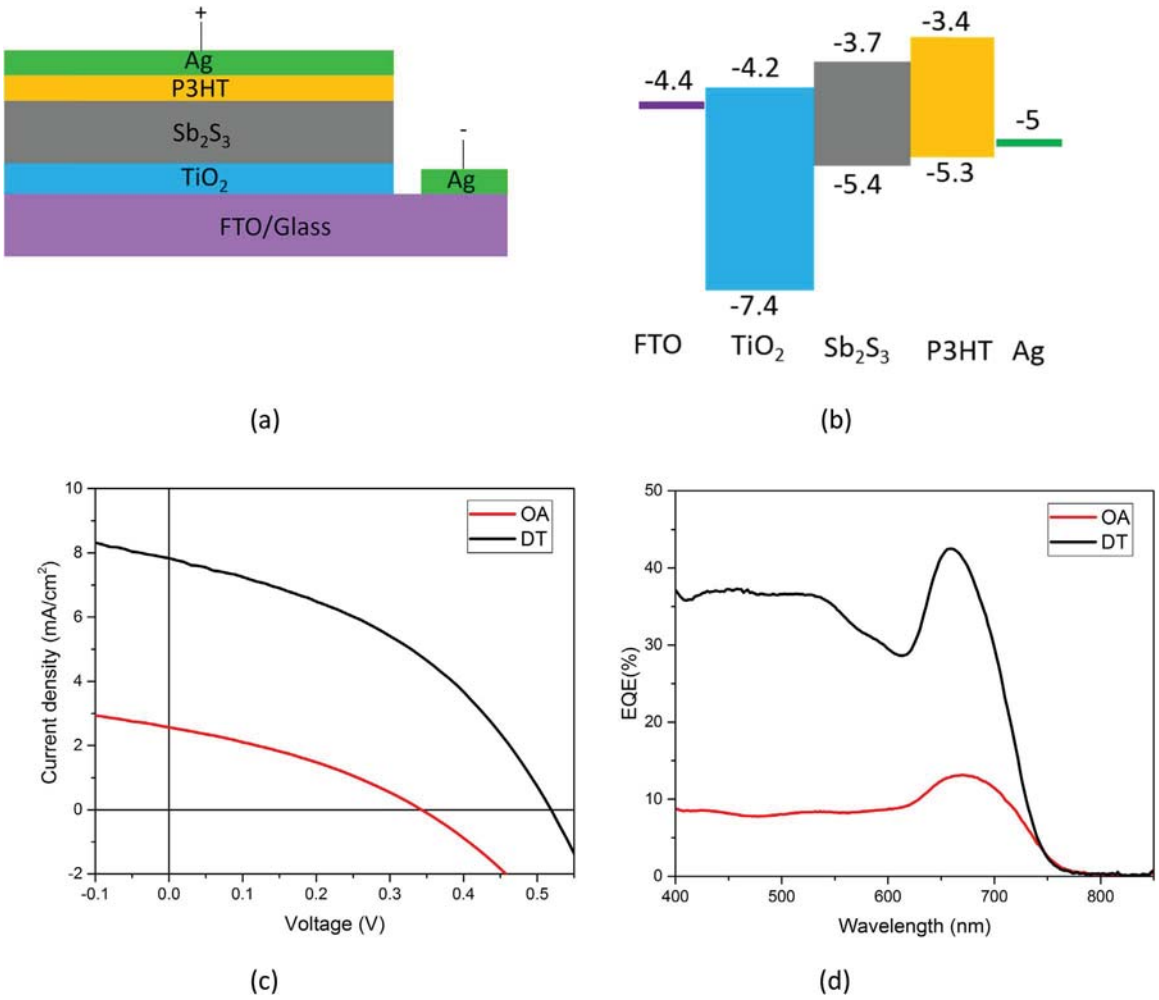

Fig. 4. (a) solar cell architecture and (b) associated energy level diagram of the used components, (c) J–V curves and (d) EQE spectra of solar cells based on the architecture shown in a) using OA (red) and DT (black) capped Sb_2S_3 nanoparticles as absorber material. (For interpretation of the references to color in this figure legend, the reader is referred to the web version of this article.)

Table 1
Photovoltaic performances of the best-performing devices based on OA and DT capped Sb_2S_3 NPs.

	V_{OC} (V)	J_{SC} (mA/cm^2)	FF (%)	PCE (%)
OA	0.35	2.67	34.2	0.30
DT	0.52	7.82	40.4	1.54

Energy levels for FTO, TiO_2, Sb_2S_3, P3HT and Ag were obtained from literature [25–28]. In this configuration, the incident light is absorbed by the Sb_2S_3 to generate electron-hole pairs, then electrons are injected from Sb_2S_3 into the TiO_2 layer and thereafter collected at the FTO electrode, while holes are extracted by P3HT and then collected at the Ag top contact. The photocurrent density-voltage (JV) curves of annealed Sb_2S_3-HSCs are shown in Fig. 4c and the photovoltaic parameters of the champion device with an efficiency of over 1.5% is summarized in Table 1. The efficiency deviations of 45 DT capped Sb_2S_3 and 25 OA capped Sb_2S_3 HSCs are shown in Fig. S2. The JV curves clearly indicate that the DT capped Sb_2S_3 HSCs generated significantly higher J_{SC} and V_{OC} values than the OA capped Sb_2S_3 HSCs. According to the results obtained from Fig. 3a, the OA ligands are still present and cover the Sb_2S_3 nanoparticles even after annealing. Thus the limited performance of OA capped Sb_2S_3 SCs can be attributed to the presence of long isolating hydrocarbon chains between Sb_2S_3 nanoparticles, as well as Sb_2S_3 and the interface layers P3HT and TiO_2, respectively. According to previous reports, both charge separation and charge transport from nanocrystal to nanocrystal are suppressed by the long chains of OA on the nanocrystal surface [10,29,30]. These chains also extend and arrange themselves in the presence of the P3HT to form an effective spacer between Sb_2S_3 and P3HT, which acts as an electrically insulating layer that impedes efficient charge transfer in the device [31]. On the contrary, the DT molecules capped on the Sb_2S_3 nanoparticles are completely removed by the annealing process (Fig. 3b), which leads to a direct contact between Sb_2S_3 nanocrystals as well as Sb_2S_3 and its interfaces to the HTM. The improved J_{SC} and V_{OC} of DT capped Sb_2S_3 HSCs indicate that the intimate contact results more efficient charge transport and charge separation in the device. However, compared with Sb_2S_3 HSCs fabricated by ALD and CBD methods [32], which also provides direct contact between Sb_2S_3 nanocrystals and Sb_2S_3/HTM layers, the best performed device in this work exhibits lower J_{SC} and V_{OC} values. This can be attributed to a high thickness variation and an insufficient surface coverage of Sb_2S_3 (Fig. 2b), which strongly increases charge recombination [25]. Actually, it is very promising, that such incomplete coverage and with thickness peaks of up to 200 nm leading to such an efficient device performance already. Our previous studies have shown, that for CBD the optimum thickness is of the Sb_2S_3 layer is below 100 nm [32,33]. In further studies, we need to carefully address, how the film can be further optimized to achieve full wetting of the substrate and better control over the film thickness to achieve the ideal thickness for efficient charge collection, which is then expected to result in significant improved device performance.

The EQE spectra of OA and DT capped Sb_2S_3 HSCs are presented in Fig. 4d. Both EQE curves show the onset of photocurrent around 750 nm, which corresponds well to the absorption edge of annealed Sb_2S_3 (Fig. 1a). The higher EQE over the full spectral range from 400 to 750 nm also indicates that the light is more efficiently converted into current by DT capped Sb_2S_3 HSCs than OA capped HSCs. For OA capped HSCs, the spectrum covers the range of 400–600 nm with EQE value of only around 10%, while for devices with ligand free Sb_2S_3 the EQE is exceeding 30% in the same range. The short circuit photocurrent under AM 1.5G generated by a solar cell can be calculated by the following equation,

$$J_{sc} = e \int \phi(\lambda) EQE(\lambda) d\lambda$$

where e is the elementary charge and $\phi(\lambda)$ is the photon flux of AM 1.5G spectrum. For the EQEs presented in Fig. 4d, the integrated J_{sc}'s for DT and OA capped HSCs are 7.66 and 2.71 mA/cm^2, respectively. These results are in good agreement with the J_{sc} values obtained from J-V measurements: 7.82 and 2.67 mA/cm^2, respectively.

In the EQE spectrum of DT capped Sb_2S_3 HSCs a depression of EQE in the range of 400–650 nm can be observed, which is especially pronounced around 600 nm. This is due to the parasitic absorption of P3HT, which competes with band-to-band absorption, decreasing the generated photocurrent in Sb_2S_3 [32]. As reported before [34], the P3HT does not contribute to the current generation, because excitons created in the P3HT layer are usually not separated into free charges, which results in geminate recombination preventing charge extraction. Even though the band alignment should enable charge separation at the Sb_2S_3 – P3HT interface, the parasitic absorption in P3HT clearly dominates over charge generation through the HTM.

4. Conclusion

In summary, novel Sb_2S_3 nanoparticle ink was prepared by using hot-injection method and DT as capping ligand. This ink was utilized in planar HSCs and compared to the commonly used capping ligand OA. With P3HT as HTM, the HSC sensitized by DT capped NPs exhibited higher efficiency (1.54% at 1 sun), short-circuit current density (7.82 mA/cm^2), open-circuit voltage (0.52 V), and fill factor (40.4%) compared to OA capped NPs. This is attributed to a complete desorption of the DT ligands after crystallization at 300 °C, which is confirmed by FTIR results, while OA molecules were only partially desorbed. Thus, improved values of short-circuit current density and open-circuit voltage of HSCs with DT capped Sb_2S_3 NPs originate from a more intimate contact across Sb_2S_3 NPs and to the interfaces. However, the SEM analysis revealed an incomplete coverage of the underlying TiO_2 layer, which lowers device characteristics compared to literature device due to increased recombination. Further optimization of ink preparation and deposition parameters are expected to improve film formation, leading to homogenously covered substrates with desired absorber thickness and improved device performance. Unfortunately, this method in its current form will not allow a low temperature fabrication (below 200 °C), as the Sb_2S_3 spheres need an annealing temperature of > 250 °C to crystallize to give efficient performance. Overall we demonstrated, that it is possible to prepare HSCs in a simple way by using a Sb_2S_3 nanoparticle ink to fabricate the absorber layer in hybrid solar cells.

Acknowledgements

The author thank David Szamosvari (AG Thomas, Biological Chemistry, Konstanz University) and Melanie Gerigk (AG Polarz, Solid-State Chemistry and Bioinorganic Chemistry, Konstanz University) for support in this work. Funding for Wei Wang is acknowledged by the China Scholarship Council (File No. 201404910464).

Appendix A. Supplementary material

Supplementary data associated with this article can be found in the online version at http://dx.doi.org/10.1016/j.solmat.2017.07.046.

References

[1] W. Xu, F. Tan, Q. Liu, X. Liu, Q. Jiang, L. Wei, W. Zhang, Z. Wang, S. Qu, Z. Wang, Efficient PbS QD solar cell with an inverted structure, Sol. Energy Mater. Sol. Cells 159 (2017) 503–509.

[2] Byungha SHIN, et al., Thin film solar cell with 8.4% power conversion efficiency using an earth-abundant Cu_2ZnSnS_4 absorber, Progress. Photovolt.: Res. Appl. 21 (1) (2013) 72–76.

[3] I. Repins, M.A. Contreras, B. Egaas, C. DeHart, J. Scharf, C.L. Perkins, B. To, R. Noufi, 19·9%-efficient ZnO/CdS/$CuInGaSe_2$ solar cell with 81.2% fill factor, Progress. Photovolt.: Res. Appl. 16 (2008) 235–239.

[4] C. Yi, X. Li, J. Luo, S.M. Zakeeruddin, M. Gratzel, Perovskite photovoltaics with outstanding performance produced by chemical conversion of bilayer mesostructured lead halide/TiO_2 films, Adv. Mater. 28 (2016) 2964–2970.

[5] Y.C. Choi, Y.H. Lee, S.H. Im, J.H. Noh, T.N. Mandal, W.S. Yang, S.I. Seok, Efficient inorganic-organic heterojunction solar cells employing $Sb_2(Sx/Se_{1-x})_3$ graded-composition sensitizers, Adv. Energy Mater. 4 (2014) 1301680.

[6] Y.C. Choi, D.U. Lee, J.H. Noh, E.K. Kim, S.I. Seok, Highly improved Sb_2S_3 sensitized-inorganic-organic heterojunction solar cells and quantification of traps by deep-level transient spectroscopy, Adv. Funct. Mater. 24 (2014) 3587–3592.

[7] D.H. Kim, S.J. Lee, M.S. Park, J.K. Kang, J.H. Heo, S.H. Im, S.J. Sung, Highly reproducible planar Sb_2S_3-sensitized solar cells based on atomic layer deposition, Nanoscale 6 (2014) 14549–14554.

[8] M. Abulikemu, S. Del Gobbo, D.H. Anjum, M.A. Malik, O.M. Bakr, Colloidal Sb_2S_3 nanocrystals: synthesis, characterization and fabrication of solid-state semiconductor sensitized solar cells, J. Mater. Chem. A 4 (2016) 6809–6814.

[9] Iwan Moreels, et al., Size-dependent optical properties of colloidal PbS quantum dots, ACS Nano 3 (10) (2009) 3023–3030.

[10] J. Tang, K.W. Kemp, S. Hoogland, K.S. Jeong, H. Liu, L. Levina, M. Furukawa, X. Wang, R. Debnath, D. Cha, K.W. Chou, A. Fischer, A. Amassian, J.B. Asbury, E.H. Sargent, Colloidal-quantum-dot photovoltaics using atomic-ligand passivation, Nat. Mater. 10 (2011) 765–771.

[11] Y. Yu, et al., High-quality ultralong Sb_2Se_3 and Sb_2S_3 nanoribbons on a large scale via a simple chemical route, J. Phys. Chem. B 110 (27) (2006) 13415–13419.

[12] E.A. El-Sayad, Compositional dependence of the optical properties of amorphous $Sb_2Se_{3-x}S_x$ thin films, J. Non-Cryst. Solids 354 (2008) 3806–3811.

[13] Zhengtao Deng, Masud Mansuripur, Anthony J. Muscat, Simple colloidal synthesis of single-crystal Sb− Se−S nanotubes with composition dependent band-gap energy in the near-infrared, Nano Lett. 9 (5) (2009) 2015–2020.

[14] P. Arun, A.G. Vedeshwar, Effect of heat treatment on the optical properties of amorphous Sb_2S_3 film: the possibility of optical storage, J. Non-Cryst. Solids 220 (1) (1997) 63–68.

[15] A.N.,C.M. Goldstein, Echer, A.P. Alivisatos, Melting in semiconductornanocrystals, Science 256 (5062) (1992) 1425–1427.

[16] H. Wedemeyer, J. Michels, R. Chmielowski, S. Bourdais, T. Muto, M. Sugiura, G. Dennler, J. Bachmann, Nanocrystalline solar cells with an antimony sulfide solid absorber by atomic layer deposition, Energy Environ. Sci. 6 (2013) 67–71.

[17] K.H. Kim, Z. Akase, T. Suzuki, D. Shindo, Charging effects on SEM/SIM contrast of metal/insulator system in various metallic coating conditions, Mater. Trans. 51 (2010) 1080–1083.

[18] D. Lee, R. Condrate, FTIR spectral characterization of thin film coatings of oleic acid on glasses: I. Coatings on glasses from ethyl alcohol, J. Mater. Sci. 34 (1999) 139–146.

[19] S. Chen, W. Liu, Oleic acid capped PbS nanoparticles: synthesis, characterization and tribological properties, Mater. Chem. Phys. 98 (2006) 183–189.

[20] L. Zhang, R. He, H.-C. Gu, Oleic acid coating on the monodisperse magnetite nanoparticles, Appl. Surf. Sci. 253 (2006) 2611–2617.

[21] C.K. Yee, A. Ulman, J.D. Ruiz, A. Parikh, H. White, M. Rafailovich, Alkyl selenide- and alkyl thiolate-functionalized gold nanoparticles: chain packing and bond nature, Langmuir: ACS J. Surf. Colloids 19 (2003) 9450–9458.

[22] T. Ang, T. Wee, W. Chin, Three-dimensional self-assembled monolayer (3D SAM) of n-alkanethiols on copper nanoclusters, J. Phys. Chem. B 108 (2004) 11001–11010.

[23] D. Xu, Z. Liu, J. Liang, Y. Qian, Solvothermal synthesis of CdS nanowires in a mixed solvent of ethylenediamine and dodecanethiol, J. Phys. Chem. B 109 (2005) 14344–14349.

[24] S. Kim, S.H. Im, M. Kang, J.H. Heo, S.I. Seok, S.W. Kim, I. Mora-Sero, J. Bisquert, Air-stable and efficient inorganic-organic heterojunction solar cells using PbS colloidal quantum dots co-capped by 1-dodecanethiol and oleic acid, Phys. Chem. Chem. Phys.: PCCP 14 (2012) 14999–15002.

[25] P.P. Boix, G. Larramona, A. Jacob, B. Delatouche, I. Mora-Seró, J. Bisquert, Hole transport and recombination in all-solid Sb_2S_3-sensitized TiO_2 solar cells using CuSCN as hole transporter, J. Phys. Chem. C 116 (2011) 1579–1587.

[26] R. Zhu, C.Y. Jiang, B. Liu, S. Ramakrishna, Highly efficient nanoporous TiO_2-polythiophene hybrid solar cells based on interfacial modification using a metal-free organic dye, Adv. Mater. 21 (2009) 994–1000.

[27] A. Le Viet, R. Jose, M. Reddy, B. Chowdari, S. Ramakrishna, Nb_2O_5 photoelectrodes for dye-sensitized solar cells: choice of the polymorph, J. Phys. Chem. C 114 (2010) 21795–21800.

[28] A. Nikolakopoulou, D. Raptis, V. Dracopoulos, L. Sygellou, K.S. Andrikopoulos,

P. Lianos, Study of upscaling possibilities for antimony sulfide solid state sensitized solar cells, J. Power Sources 278 (2015) 404–410.
[29] Mohammad H. Zarghami, et al., p-Type PbSe and PbS quantum dot solids prepared with short-chain acids and diacids, ACS Nano 4 (4) (2010) 2475–2485.
[30] C.H. Chuang, P.R. Brown, V. Bulovic, M.G. Bawendi, Improved performance and stability in quantum dot solar cells through band alignment engineering, Nat. Mater. 13 (2014) 796–801.
[31] L. Schmidt-Mende, J.E. Kroeze, J.R. Durrant, M.K. Nazeeruddin, M. Grätzel, Effect of hydrocarbon chain length of amphiphilic ruthenium dyes on solid-state dye-sensitized photovoltaics, Nano Lett. 5 (2005) 1315–1320.
[32] E. Zimmermann, T. Pfadler, J. Kalb, J.A. Dorman, D. Sommer, G. Hahn, J. Weickert, L. Schmidt-Mende, Toward high-efficiency solution-processed planar heterojunction Sb_2S_3 solar cells, Adv. Sci. 2 (2015) 1500059.
[33] T. Pfadler, M. Stärk, E. Zimmermann, M. Putnik, J. Boneberg, J. Weickert, L. Schmidt-Mende, A comparison of light-coupling into high and low index nanostructured photovoltaic thin films, APL Mater. 3 (2015) 066101.
[34] E. Kärber, A. Katerski, I.O. Acik, A. Mere, V. Mikli, M. Krunks, Sb_2S_3 grown by ultrasonic spray pyrolysis and its application in a hybrid solar cell, Beilstein J. Nanotechnol. 7 (2016) 1662–1673.